

through the fluid medium.

A. The standard IBM

The standard formulation of the IBM²⁰ applies to a droplet embedded in a homogeneous incompressible fluid of density ρ and dynamic viscosity η . The droplet's surface, $\mathbf{X}(\mathbf{q})$, is parameterized by curvilinear coordinates, \mathbf{q} , and is discretized into a set of markers, $\{\mathbf{X}_i\}$, at fixed material points along the boundary, as shown schematically in Fig. 1.

The fluid flow, $\mathbf{u}(\mathbf{x}_j)$, and pressure, $p(\mathbf{x}_j)$, are defined on a Cartesian grid, \mathbf{x}_j , with uniform spacing h , and are governed by the viscous, incompressible Navier-Stokes equations,

$$\rho (\partial_t + \mathbf{u} \cdot \nabla) \mathbf{u} = -\nabla p + \eta \nabla^2 \mathbf{u} + \mathbf{f} \quad (1a)$$

$$\nabla \cdot \mathbf{u} = 0. \quad (1b)$$

By Newton's third law, the force on the fluid element at \mathbf{x}_j ,

$$\mathbf{f}(\mathbf{x}_j, t) = - \int \mathbf{F}(\mathbf{q}, t) \delta_h(\|\mathbf{x}_j - \mathbf{X}(\mathbf{q}, t)\|) d\mathbf{q}, \quad (2)$$

is equal and opposite to the local force on the boundary, $\mathbf{F}(\mathbf{q}, t)$, due to surface tension and the influence of external fields. The kernel, δ_h , interpolates over the markers, \mathbf{X}_i , in the neighborhood of a discrete gridpoint, \mathbf{x}_j . Likewise, each massless boundary marker is advected by the fluid at a velocity

$$\mathbf{U}_i = \int \mathbf{u}(\mathbf{x}_j, t) \delta_h(\|\mathbf{x}_j - \mathbf{X}_i\|) d\mathbf{x}_j \quad (3)$$

that is interpolated from the computational grid.

The IBM defined by Eqs. (1)-(3) generally proceeds in a cycle, as depicted in Fig. 2. Given an initial droplet shape, $\{\mathbf{X}_i\}$, the forces, $\{\mathbf{F}_i\}$, on the boundary markers are calculated from the combined influences of surface tension and external forces. The complementary force field acting on the fluid, $\mathbf{f}(\mathbf{x}_j, t)$, is then computed with Eq. (2). The Navier-Stokes equations, Eq. (1), then are solved numerically^{19,20} to obtain the updated fluid velocity, $\mathbf{u}(\mathbf{x}_j, t)$. Finally, Eq. (3) is used to determine the no-slip motion of the boundary, $\partial_t \mathbf{X} = \mathbf{U}$, and the procedure is repeated for the updated boundary configuration, $\{\mathbf{X}_j\}$.

In this work, we implement the same numerical scheme first introduced by Peskin¹⁹, using the spacial and temporal discretizations and four-point discrete delta function described in Sections 4-7 of Ref.²⁰. To improve volume conservation, we calculate the fluid fields on a staggered, marker-and-cell grid²⁴.

B. Penalty IBM for Massive Droplets

The standard IBM cannot account for multiphase flows where properties of the droplet, such as density and viscoelasticity, differ from those of the surrounding medium²⁴. For simplicity, we focus on the droplet's density contrast relative

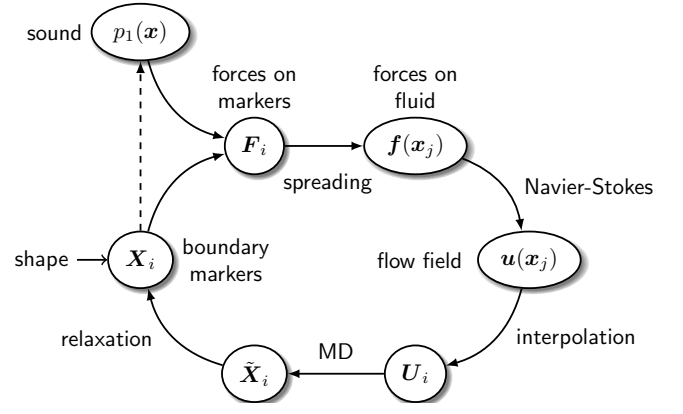


FIG. 2. Immersed Boundary Method for acoustic manipulation of deformable objects.

to the medium. To incorporate the droplet's excess mass, we implement an extension of the IBM based on the penalty Immersed Boundary Method^{22,25}.

The penalty IBM models the density of the droplet interior by introducing a set of massless tracer particles at locations $\{\mathbf{X}_i^m\}$ whose trajectories trivially satisfy Eqs. (1)-(3). As shown in Fig. 1, each of these fluid markers is coupled to a corresponding *mass marker* at position \mathbf{Y}_i^m by a spring of stiffness K_P . The i -th fluid marker experiences a force,

$$\mathbf{F}_i^m = K_P (\mathbf{Y}_i^m - \mathbf{X}_i^m), \quad (4)$$

that accelerates it according to Newton's second law,

$$M \partial_t^2 \mathbf{Y}_i^m = -\mathbf{F}_i^m - M g \hat{z}, \quad (5)$$

where M is the marker's mass and g is the acceleration due to gravity.

In theory, the fluid markers and mass markers ought to coincide in the limit of large K_P . In practice, however, numerical instability arises when K_P is too large. Consequently, K_P is chosen phenomenologically to maintain pair separations smaller than the computational grid size, typically at $h/10$.

C. Surface Tension

The internal boundary stress on a marker at \mathbf{X}_i is often formulated as a restoring force, $\mathbf{F}_i = -\delta_{\mathbf{X}_i} E$, that minimizes the interfacial energy, $E[\{\mathbf{X}_j\}]$. When this approach is used to model surface tension, the interfacial energy is proportional to the droplet's total surface area. In two dimensions, it is proportional to the length of the interface,

$$E[\{\mathbf{X}_j\}] = \sigma A = \sigma \sum_{j=1}^{N_{ib}-1} \|\ell_j\|, \quad (6)$$

where $\ell_j \equiv \mathbf{X}_{j+1} - \mathbf{X}_j$, and σ is the interfacial tension. The force of surface tension acting on the marker is then

$$\mathbf{F}_i^\sigma \left(\sigma \sum_{j=1}^{N_{ib}-1} \|\ell_j\| \right) = -\sigma (\hat{\ell}_i - \hat{\ell}_{i-1}). \quad (7)$$

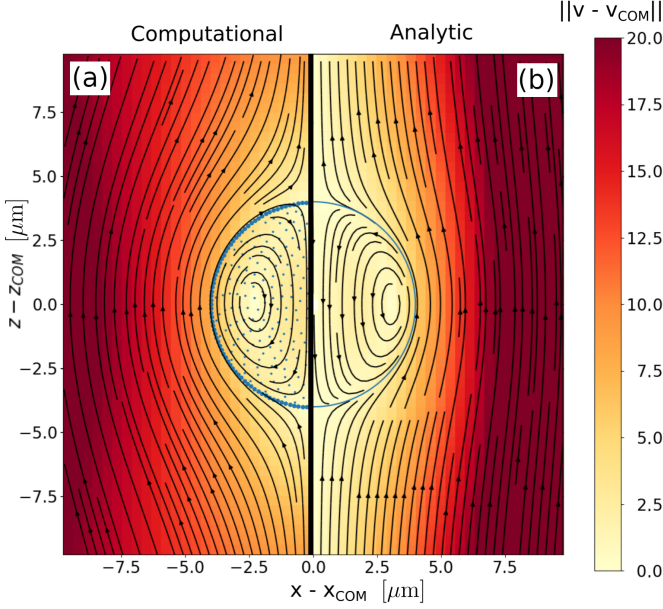


FIG. 3. Streamlines within and around a 4 μm droplet falling through an unbounded fluid at its terminal velocity, $\approx 20 \mu\text{m s}^{-1}$. We compare the analytic stream function from Happel and Brenner²⁶ (left) to simulations using a penalty immersed boundary method for the droplet's excess mass (right).

Equation (7) correctly models surface tension if the boundary markers are uniformly distributed around the droplet's boundary. To this end, the markers are redistributed tangentially along the boundary at each time step.

Surface tension exerts a normal on the droplet surface to minimize local curvature. Consequently, Eq. (7) also defines the surface normal, $\hat{\mathbf{n}}_i = \mathbf{F}_i^\sigma / \|\mathbf{F}_i^\sigma\|$.

D. Benchmark: Sedimenting Droplet

To demonstrate and benchmark our implementation of the IBM, we model the sedimentation of a droplet in an unbounded fluid²³. Figure 3 presents a cross-section of the flow around and within a droplet of radius $R = 4 \mu\text{m}$ and buoyant density $\rho_p - \rho_0 = 0.18 \text{ g cm}^{-3}$, which corresponds to silicone oil sedimenting in water⁵. For simplicity, we assume the fluid droplet has the same viscosity as the surrounding medium. The plot shows streamlines of the flow in the co-moving frame and is colored by the local flow speed. The data in Fig. 3(a) are computed with the IBM in a $20 \mu\text{m} \times 20 \mu\text{m}$ periodic domain. They are compared side-by-side with the analytic result for a spherical droplet²⁶ in Fig. 3(b). This solution for the two-phase flow is reproduced in Appendix A.

Slight differences between the two flow fields can be attributed to the influence of periodic boundary conditions on the simulations and to the implicit assumption of infinite surface tension in the analytic model.

III. ACOUSTICS

The standard IBM relies on the incompressible Navier-Stokes equations, Eq. (1), and therefore does not accommodate sound waves. Describing the fields within an acoustic levitator requires the compressible Navier-Stokes equations,

$$\partial_t \rho = -\nabla \cdot (\rho \mathbf{u}) \quad (8a)$$

$$\rho (\partial_t + \mathbf{u} \cdot \nabla) \mathbf{u} = -\nabla p + \eta \nabla^2 \mathbf{u} + \beta \eta \nabla (\nabla \cdot \mathbf{u}), \quad (8b)$$

where $\beta = \xi/\eta + 1/3$ incorporates the fluid's volume viscosity, ξ ^{14,27}.

In the absence of sound waves, the fluid medium is quiescent, $\mathbf{u} = 0$, and has uniform pressure p_0 , and uniform density, ρ_0 . An acoustic levitator projects a time-harmonic pressure wave, $p_{\text{inc}}(\mathbf{x}, t) = p_{\text{inc}}(\mathbf{x}) \exp(-i\omega t)$, into the fluid. The droplet scatters a portion of p_{inc} to create a scattered wave, $p_{\text{scat}}(\mathbf{x}, t) = p_{\text{scat}}(\mathbf{x}, \{\mathbf{X}_j\}) \exp(-i\omega t)$, that depends on the position and shape of the droplet. The incident and scattered waves together cause small pressure fluctuations, $p_1(\mathbf{x}) = p_{\text{inc}}(\mathbf{x}) + p_{\text{scat}}(\mathbf{x})$, about p_0 . This first-order pressure wave is associated with a first-order density wave, $\rho_1(\mathbf{x})$, and a first-order velocity field, $\mathbf{u}_1(\mathbf{x})$, that are obtained by expanding Eq. (8) to first order in the fields.

Acoustic levitators typically operate at such high frequencies that the period of $p_1(\mathbf{x}, t)$ is much shorter than the viscous and inertial time scales that govern droplet dynamics and streaming flows. Those comparatively slow processes emerge as averages over multiple acoustic cycles. Because the first-order fields are harmonic and therefore vanish on average, standard acoustic perturbation theory⁹ expands the density, pressure and velocity fields to second order:

$$\rho = \rho_0 + \rho_1 + \rho_2 \quad (9a)$$

$$p = p_0 + p_1 + p_2 \quad (9b)$$

$$\mathbf{u} = \mathbf{u}_1 + \mathbf{u}_2. \quad (9c)$$

The second-order fields, ρ_2 , p_2 and \mathbf{u}_2 , do not vanish on average, and therefore describe steady dynamics that persist on hydrodynamic timescales and therefore account for the droplet's macroscopic behavior.

We extend the IBM to incorporate sound waves by identifying the time-averaged acoustic radiation force on each element of the droplet surface^{6,7,9,28,29}:

$$\mathbf{F}_i^{\text{ARF}}(t) = -\langle p_2 \rangle \hat{\mathbf{n}} - \rho_0 \langle (\mathbf{u}_1 \cdot \hat{\mathbf{n}}) \mathbf{u}_1 \rangle, \quad (10)$$

where the continuous fields are evaluated at $\mathbf{x} = \mathbf{X}_i$ and angle brackets represent an average over one acoustic cycle. The first term on the right-hand side of Eq. (10) describes acoustic radiation pressure, and the second term arises from advection of fluid by the droplet's oscillating boundary^{7,28}.

The net force on the boundary marker at \mathbf{X}_i ,

$$\mathbf{F}_i(t) = \mathbf{F}_i^{\text{ST}}(t) + \mathbf{F}_i^{\text{ARF}}(t), \quad (11)$$

is the sum of the surface tension from Eq. (7) and the time-averaged acoustic force from Eq. (10). The interfacial force

drives streaming flows, $\langle \mathbf{u}(\mathbf{x}_j, t) \rangle = \mathbf{u}_2(\mathbf{x}, t)$, and shape deformations, $\partial_t \mathbf{X}_i = \mathbf{U}_i$, through the cycle depicted in Fig. 2. This extension to the incompressible IBM is one of the principal contributions of the present work. Its implementation requires expressions for the first- and second-order fields.

A. First-Order Equations for the Acoustic Wave

The first-order Navier-Stokes equations,

$$\partial_t \rho_1 = -\rho_0 \nabla \cdot \mathbf{u}_1 \quad (12a)$$

$$\rho_0 \partial_t \mathbf{u}_1 = -\nabla p_1 + \eta (\beta + 1) \nabla (\nabla \cdot \mathbf{u}_1) - \eta \nabla \times \nabla \times \mathbf{u}_1, \quad (12b)$$

can be simplified to a pair of wave equations,

$$\nabla^2 \phi = -\frac{k^2}{\gamma} \phi \quad (13a)$$

$$\nabla \times \nabla \times \psi = k_v^2 \psi, \quad (13b)$$

by introducing the Helmholtz decomposition,

$$\mathbf{u}_1(\mathbf{r}) = \nabla \phi + \nabla \times \psi, \quad (14a)$$

$$p_1(\mathbf{r}) = \frac{i\omega\rho_0}{\gamma} \phi(\mathbf{r}), \quad (14b)$$

and noting that $p_1(\mathbf{r}) = c_0^2 \rho_1(\mathbf{r})$ in an isentropic fluid medium with speed of sound c_0 . Equation (13a) describes a scalar pressure wave that propagates with the acoustic wavenumber, $k = \omega/c_0$. Likewise, Eq. (13b) describes vortical waves that carry away the acoustic energy lost to viscous damping. The acoustic damping coefficient,

$$\gamma = 1 + (\beta + 1) \left(\frac{k}{k_v} \right)^2, \quad (15)$$

and the viscous wave number,

$$k_v = \frac{1+i}{\delta}, \quad (16)$$

are both characterized by the thickness of the viscous boundary layer²⁷,

$$\delta(\omega) = \sqrt{\frac{2\eta}{\rho_0 \omega}}. \quad (17)$$

Following conventional acoustic radiation theory^{5,27}, we neglect viscosity in the first-order fields, so that $\gamma \approx 1$ and $\psi \approx \mathbf{0}$. The solution to Eq. (13) can then be found by a multipole expansion of $\phi(\mathbf{r})$ both inside and outside the droplet³⁰,

$$\phi_I(\mathbf{r}) = \phi_0 \sum_{\ell=0}^{\infty} \sum_{m=-\ell}^{\ell} b_{\ell}^m j_{\ell}(k_I r) P_{\ell}^m(\cos \theta) \quad \text{and} \quad (18a)$$

$$\phi_O(\mathbf{r}) = \phi_0 \sum_{\ell=0}^{\infty} \sum_{m=-\ell}^{\ell} a_{\ell}^m [j_{\ell}(kr) + s_{\ell}^m h_{\ell}(kr)] P_{\ell}^m(\cos \theta), \quad (18b)$$

respectively, where j_{ℓ} and h_{ℓ} are the spherical Bessel and Hankel functions, respectively, and P_{ℓ}^m is the associated Legendre polynomial. Distances in Eq. (18a) are scaled by the wavenumber inside the droplet, $k_I = \omega/c_I$.

The beam-shape coefficients, a_{ℓ}^m , depend on the structure of the incident sound wave, which typically is known *a priori*. The scattering coefficients, s_{ℓ}^m and b_{ℓ}^m , are obtained by satisfying boundary conditions at the droplet surface,

$$p_I = p_O \quad \text{and} \quad (19a)$$

$$\mathbf{u}_I \cdot \hat{\mathbf{n}} = \mathbf{u}_O \cdot \hat{\mathbf{n}}. \quad (19b)$$

For a spherical droplet of radius R , which is the simplest case, the scattering coefficients reduce to

$$b_{\ell}^m = \tilde{\rho} a_{\ell}^m \left[\frac{j_{\ell}(kR)}{j_{\ell}(k_I R)} + s_{\ell}^m \frac{h_{\ell}(kR)}{j_{\ell}(k_I R)} \right] \quad \text{and} \quad (20a)$$

$$s_{\ell}^m = -\frac{\tilde{\rho} \tilde{c} j_{\ell}(kR) j'_{\ell}(k_I R) - j_{\ell}(k_I R) j'_{\ell}(kR)}{\tilde{\rho} \tilde{c} h_{\ell}(kR) j'_{\ell}(k_I R) - j_{\ell}(k_I R) h'_{\ell}(kR)}, \quad (20b)$$

where $\tilde{\rho} = \rho_O/\rho_I$ and $\tilde{c} = k_I/k = c_O/c_I$, and primes denote derivatives with respect to the argument. In the special case $\tilde{c} = 1$, the scattering coefficients simplify further to

$$b_{\ell}^m = \tilde{\rho} a_{\ell}^m \left[1 + s_{\ell}^m \frac{h_{\ell}(kR)}{j_{\ell}(kR)} \right] \quad \text{and} \quad (21a)$$

$$s_{\ell}^m = -\frac{\tilde{\rho} - 1}{\tilde{\rho} \frac{h_{\ell}(kR)}{j_{\ell}(kR)} - \frac{h'_{\ell}(kR)}{j'_{\ell}(kR)}}. \quad (21b)$$

Equations (20) and (21) serve as a point of departure for describing scattering by aspherical droplets.

B. Second-Order Equations for Time-Averaged Dynamics

The first-order incident and scattered sound waves together give rise to steady forces and flows at second order. The steady, time-averaged second-order Navier-Stokes equations,

$$-\nabla \cdot \langle \rho_1 \mathbf{u}_1 \rangle = \rho_0 \langle \nabla \cdot \mathbf{u}_2 \rangle \quad (22a)$$

$$\langle \rho_1 \partial_t \mathbf{u}_1 + \rho_0 (\mathbf{u}_1 \cdot \nabla) \mathbf{u}_1 \rangle = -\nabla \langle p_2 \rangle + \eta \nabla^2 \langle \mathbf{u}_2 \rangle + \beta \eta \nabla \langle \nabla \cdot \mathbf{u}_2 \rangle, \quad (22b)$$

reduce to

$$-\nabla \langle p_2 \rangle + \eta \nabla \times \langle \nabla \times \mathbf{u}_2 \rangle = \mathbf{f}_R \quad (23)$$

in the limit that the fluid is incompressible, $\langle \nabla \cdot \mathbf{u}_2 \rangle = 0$ ³¹. The Reynolds stress that drives the flow,

$$\mathbf{f}_R(\mathbf{r}) \equiv \rho_0 \nabla \cdot \langle \mathbf{u}_1 \mathbf{u}_1 \rangle, \quad (24)$$

is obtained from the first-order solution. The acoustic radiation pressure, $\langle p_2 \rangle$, and vortical acoustic streaming, $\langle \nabla \times \mathbf{u}_2 \rangle$, are given by the irrotational and solenoidal components of \mathbf{f}_R , respectively. The latter term vanishes because we neglect viscosity in the first-order fields, which means that $\mathbf{u}_1(\mathbf{r}) = \nabla \phi$

and therefore that the Reynolds stress is irrotational. Consequently, the viscous flows described by the second term on the left-hand side of Eq. (23) vanish. From this, we conclude that the radiation pressure is^{9,16}

$$\langle p_2 \rangle = \frac{1}{2} \rho_0 \langle u_1^2 \rangle - \frac{1}{2} \kappa_0 \langle p_1^2 \rangle, \quad (25)$$

where $\kappa_0 = (\rho_0 c_0^2)^{-1}$ is the isentropic compressibility of the fluid. The second-order pressure wave depends on the squares of the first-order fields and therefore does not vanish on an average over the acoustic period. It nevertheless can vary on inertial time scales.

When the boundary layer is thin, $\delta(\omega) \ll R$, Eq. (25) is a good approximation for $\langle p_2 \rangle$ evaluated at the time-averaged position of the droplet surface, and therefore completes the description of the sound wave required to model the acoustic force acting on the droplet through Eq. (10). While we have neglected viscous streaming due to the Reynolds stress, $\mathbf{f}_R(\mathbf{r})$, in Eq. (24), our simulations still have acoustic streaming flows that are driven by the momentum flux advected by the boundary, which is described by the second term on the right-hand side of Eq. (10).

C. Acoustic Radiation Force on an Ellipsoid

Together, Eq. (10) and Eq. (25) express the second-order acoustic radiation force on the droplet in terms of first-order acoustic fields. Analytic solutions for these first-order fields are known for certain geometries with high symmetry. More generally, the scattering coefficients in Eq. (18) may be obtained via a variety of semi-analytic techniques. These include the T-matrix method, which has been extended to acoustics by Waterman¹⁸, the discrete dipole approximation³², and modal-matching methods^{17,33}. Here, we introduce an alternative approximation scheme that leverages the exact spherical solution and consequently is more efficient when deformations are small.

1. Approximate solutions for slightly aspherical droplets

To leading order, the fields scattered by a slightly aspherical droplet are approximated by the fields scattered by the minimally enclosing sphere. The simple spherical approximation, however, does not satisfy the appropriate boundary conditions for the fluid velocity at the droplet's surface,

$$[\mathbf{u}_O(\mathbf{r}_s) - \mathbf{u}_I(\mathbf{r}_s)] \cdot \hat{\mathbf{n}}(\mathbf{r}_s) = 0 \quad (26a)$$

$$[\tilde{\rho} \mathbf{u}_O(\mathbf{r}_s) - \mathbf{u}_I(\mathbf{r}_s)] \cdot \hat{\mathbf{t}}(\mathbf{r}_s) = 0, \quad (26b)$$

where $\hat{\mathbf{t}}$ is the surface tangent unit vector, and $\hat{\mathbf{t}} \times \hat{\mathbf{n}} = 0$. Taking $\mathbf{U}(\mathbf{r})$ to be the flow field that would be created by the enclosing sphere, the actual flow field at position \mathbf{r}_s on the surface of the distorted sphere can be approximated by

$$\mathbf{u}_I(\mathbf{r}_s) = \mathbf{U}_I(\mathbf{r}_s), \quad (27a)$$

$$\mathbf{u}_O(\mathbf{r}_s) = \mathbf{U}_O(\mathbf{r}_s) + \delta(\mathbf{r}_s). \quad (27b)$$

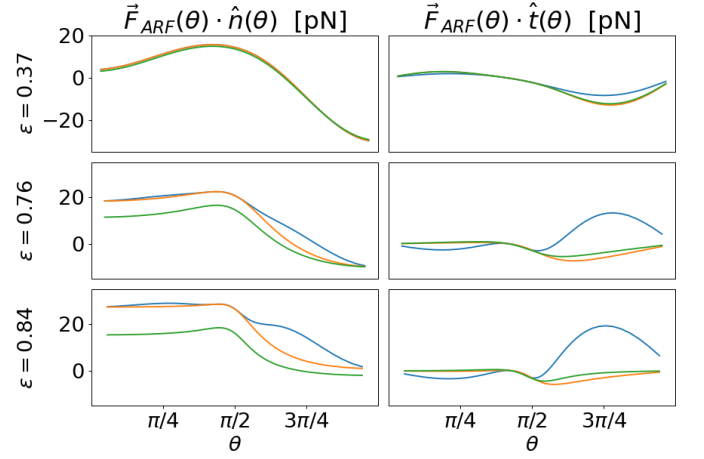


FIG. 4. ARF profile from $\theta \in [0, \pi]$ for ellipsoids of various eccentricities at a displacement from the node of $z_0 = -0.6 \mu\text{m}$. The ARF at the surface is calculated using the spherical fields from Eq. (21) (blue), the projection correction described in Eq. (26) (orange), and the exact analytic solution in spheroidal coordinates (green).

This flow field satisfies the boundary conditions in Eq. (26) if

$$\delta(\mathbf{r}_s) \cdot \hat{\mathbf{r}} = n_\theta(\mathbf{r}_s) \left(1 - \frac{1}{\tilde{\rho}} \right) \mathbf{U}_I(\mathbf{r}_s) \cdot \hat{\mathbf{t}}(\mathbf{r}_s), \quad \text{and} \quad (28a)$$

$$\delta(\mathbf{r}_s) \cdot \hat{\boldsymbol{\theta}} = n_\theta(\mathbf{r}_s) \left(1 - \frac{1}{\tilde{\rho}} \right) \mathbf{U}_I(\mathbf{r}_s) \cdot \hat{\mathbf{n}}(\mathbf{r}_s), \quad (28b)$$

where $n_\theta \equiv \hat{\mathbf{n}}(\mathbf{r}_s) \cdot \hat{\boldsymbol{\theta}}$.

The velocity field obtained with Eq. (28) does not necessarily satisfy the Helmholtz equation, nor is it necessarily curl-free. Both of these conditions are *approximately* satisfied, however, so long as the droplet's distortions are small, $n_\theta \ll 1$. Moreover, $\mathbf{u}(\mathbf{r})$ satisfies the boundary conditions from Eq. (19), and therefore should accurately represent the induced flow near the droplet's surface.

2. Comparison to analytic solution for an ellipsoid

We test this approximation scheme on the special case of spheroidal droplets, whose scattering coefficients can be expressed analytically in spheroidal coordinates³⁰. The associated spheroidal wave functions are much more costly to evaluate than spherical harmonics, which limits the utility of the analytic solution for time-resolved simulations. Analytic solutions for spheroids are useful, nonetheless, for validating our computationally efficient approximation scheme.

Figure 4 compares analytic and approximated force profiles computed for spheroids of various eccentricities. Each spheroid is taken to be displaced by $z_0 = -0.6 \mu\text{m}$ from the node of a standing wave; the influence of the droplet's displacement is discussed further in Appendix B. The spherical solution, $\mathbf{u}_O(\mathbf{r}_s) = \mathbf{U}_O(\mathbf{r}_s)$, plotted in blue, has qualitatively different behavior from the true solution, plotted in green,

even at small deformations. By contrast, the corrected solutions, $\mathbf{u}_O(\mathbf{r}_S) = \mathbf{U}_O(\mathbf{r}_S) + \delta(\mathbf{r}_S)$, plotted in orange, agrees with analytic radiation force for moderate deformations. The normal component of the computed force tracks the functional form of the exact solution up to a reasonably small multiplicative factor. This discrepancy should not significantly affect the shape or dynamics of the droplet, which is assumed to be incompressible. Agreement with the analytic solution is much better for the tangential forces, which are responsible for driving acoustic streaming flows in our simulations. The hybrid IBM therefore should predict the structure of streaming flows far more accurately than the simple spherical approximation, and far more efficiently than the analytic solution. A further discussion of limitations of Eq. (28) is provided in Appendix B.

IV. RESULTS: DROPLET IN A STANDING PLANE WAVE

Section II introduces an IBM that models the dynamics of a droplet suspended in a fluid under the general influence of external forces. Section III explains how sound propagating through the fluid generates such forces. Purely analytic solutions to the sound-driven moving-boundary problem are not yet available. Any purely numerical description of the sound wave^{34,35} would have to iterate through an enormous range of time scales to capture the moving droplet's steady dynamics. Our hybrid implementation describes the sound wave semi-analytically and handles the moving-boundary problem numerically. The result is an accurate and exceptionally efficient implementation.

We demonstrate the efficacy of the hybrid IBM with an illustrative model system: a single droplet levitated in a planar acoustic standing wave. To set up the IBM for this system, we specify the standing wave's scalar potential,

$$\phi_i(\mathbf{r}) = \phi_0 \sin(kz), \quad (29)$$

with amplitude ϕ_0 and a nodal plane at $z = 0$. The associated beam-shape coefficients⁶,

$$a_\ell^m = (2\ell + 1) \cos\left(kz + \frac{\ell\pi}{2}\right). \quad (30)$$

yield a compact expression for the the net ARF on the droplet:

$$\sum_{i=0}^{N_b} \mathbf{F}_i^{ARF} = \frac{1}{2} \rho_0 \phi_0^2 Q \sin(2kz) \hat{z}, \quad (31)$$

where the radiation force efficiency, Q , is a dimensionless scattering coefficient that depends on droplet geometry and boundary conditions^{5,6}. For a rigid sphere in a standing wave, $Q = k^3 V_p / 5^6$, and V_p is the volume of the particle. The scale of the acoustic force, $\frac{1}{2} \rho_0 \phi_0^2$, is set by the driving voltage in experimental realizations⁵.

The simulations described in this section all start with a spherical droplet of radius $R = 2\mu\text{m}$ and density $\rho_I = 1.18\text{g cm}^{-3}$, dispersed in water. The droplet is subject to a buoyant force, $F_g = (\rho_I - \rho_0) V_p g \approx 60\text{pN}$, that is balanced

by acoustic forces. To model practical acoustic levitators for water-borne samples⁵, the driving frequency is set to 2 MHz. The dimensionless size parameter, $kR = 0.034$, is well within the Rayleigh limit, $kR \ll 1$. The droplet initially is released at the nodal plane, and then relaxes to its equilibrium position, z_0 , and to its equilibrium shape.

A. Separation of Timescales

Modelling a levitated droplet illustrates the advantages of our hybrid method relative to conventional numerical techniques. The acoustic IBM presented in Ref.⁸, for example, computes the influence of acoustic forces by directly solving the compressible Navier-Stokes equations using a 5th-order Weighted Essentially Non Oscillatory (WENO) scheme. When applied to a system that is comparable to ours³⁴, the WENO scheme numerically resolves acoustic wave propagation with timestep $dt \approx R/c \approx 1.33\text{ns}$. By treating acoustic-scale processes semi-analytically, the hybrid IBM can resolve the droplet's dynamics with time steps of $15\mu\text{s}$, which represents an inherent ten-thousand-fold improvement in efficiency.

B. Equilibrium Shape of a Levitated Droplet

The equilibrium shape of a droplet in an acoustic field is typically found analytically^{36,37} by relating the surface curvature to acoustic stresses with the Young-Laplace formula. Working in two dimensions, the equilibrium shape of a slightly deformed droplet of radius R may be expanded in associated Legendre polynomials¹⁵,

$$r(\theta) = R + \sum_{\ell=0}^{\infty} \sum_{m=-\ell}^{\ell} x_{\ell m} P_\ell^m(\cos \theta). \quad (32)$$

When the droplet has the same viscosity as the medium, the normal force, $F_n(\theta) = \mathbf{F}^{ARF} \cdot \hat{n}$, determines the static shape deformation^{15,38},

$$x_{\ell m} = \frac{R^2}{(\ell+2)(\ell-1)\sigma} \int_{-1}^1 F_n(\theta) P_\ell^m(\cos \theta) d \cos \theta. \quad (33)$$

In a standing wave, the primary deformation mode is described by x_{20} , which flattens the droplet into a roughly elliptical shape. Figure 7 compares the value for x_{20} observed in IBM simulations of a droplet of $R = 2\mu\text{m}$ with predictions of Eq. (33) over a range of values of surface tension, σ , and trap strength, ϕ_0^2 . The computed deformation agrees well for droplets close to the trapping plane, and deviates at larger displacements from the node. This is because our approximation for scattering, Sec. III C 1, begins to break down at larger displacements from the node.

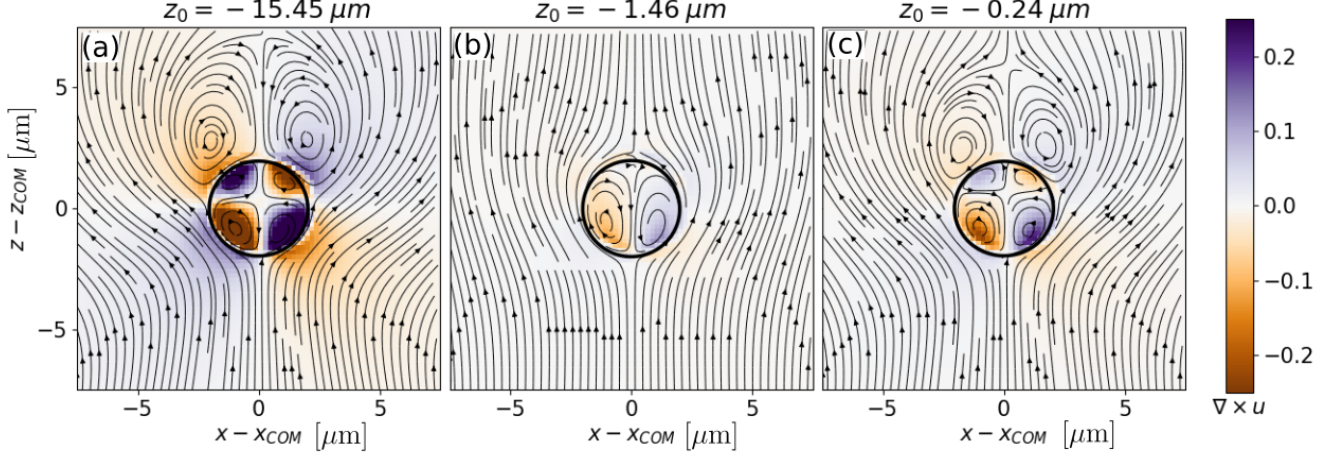


FIG. 5. Streaming profiles for a droplet levitated in water with $\sigma = 3.3 \text{ nN}\mu\text{m}^{-1}$ and $R = 2 \mu\text{m}$ at various trap strengths. (a) Gravity displaces the droplet downward from the nodal plane, favoring quadrupolar streaming in the weakest levitator. (b) Increasing trap strength induces a crossover to dipolar streaming. (c) Increasing trap strength further induces a second crossover to quadrupolar flow. The flow's vorticity is indicated by color.

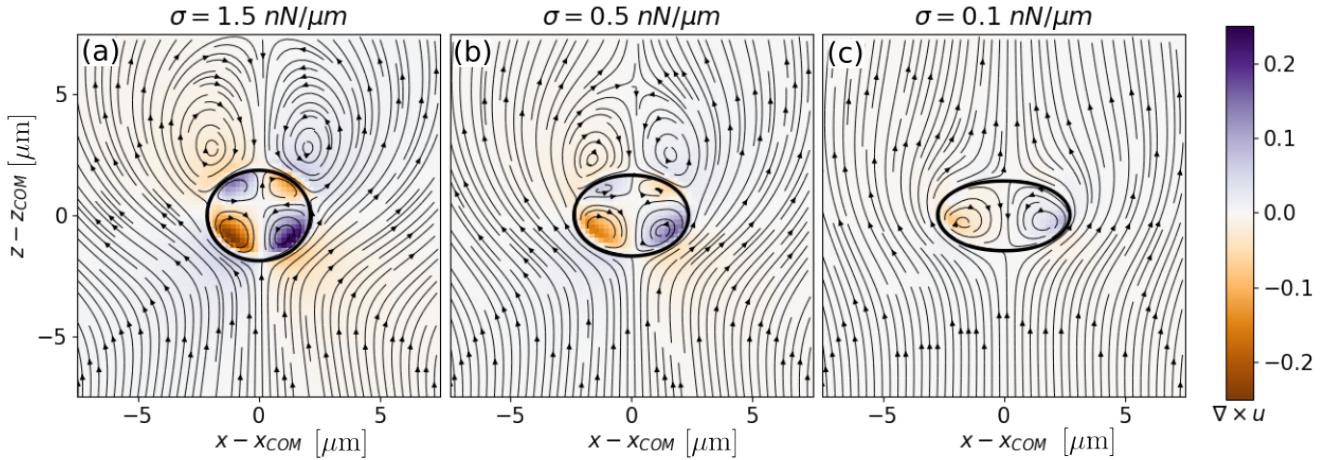


FIG. 6. Streamlines of the streaming flow for a droplet of radius $R = 2 \mu\text{m}$ in a strong levitator, $z_0 \approx -0.15 \mu\text{m}$. (a) Reducing the surface tension, σ , by half relative to Fig. 5 allows the droplet to deform while retaining quadrupolar flows. (b) Further reducing surface tension increases the droplet's distortion while significantly decreasing the vorticity in the streaming flow. (c) A highly deformable droplet induces dipolar streaming flows.

C. Acoustic Streaming

Acoustic forces not only translate and deform the droplet, but also generate interior and exterior streaming flows. In the case of a spherical droplet, these flow fields can be described analytically. The streaming profiles for an acoustically levitated droplet are characterised by a transition from dipolar flow to quadrupolar flow depending on the relative magnitude of acoustically-driven pulsation and translation modes respectively¹⁴. The streaming behavior depends on properties of the droplet and surrounding fluid, and can also be manipulated directly by adjusting the sound intensity, ϕ_0^2 , of the trap to control the droplet's position relative to the node.

1. Spherical Droplet

The streaming profiles around a spherical droplet have been computed analytically by Baasch, Doinikov, and Dual in Ref.¹⁴. Their solution should be comparable to results of the hybrid IBM under conditions where shape deformations are small, *i.e.* $\sigma R \gg \rho_0 \phi_0^2$. The results in Fig. 5 are obtained by fixing the surface tension at a fairly large value, $\sigma = 3.3 \text{ nN}\mu\text{m}^{-1}$, and varying the trap strength, ϕ_0^2 . Because the droplet is more dense than its medium, it sinks below the nodal plane by a distance that is inversely proportional to the traps' strength and therefore samples different regions of the acoustic force landscape. This has consequences for the na-

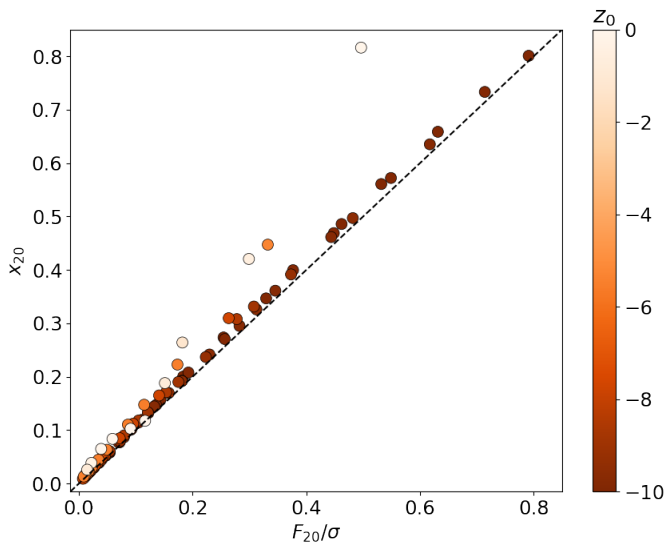


FIG. 7. Dependence of a droplet's degree of deformation on the relative strength of the acoustic driving. Outliers represent droplets that were not stably trapped.

ture of the induced streaming flow.

Figure 5(a) shows the quadrupolar streaming flow that is induced when the droplet is far below the nodal plane in a comparatively weak acoustic trap. Increasing ϕ_0 by a factor of 3 in Fig. 5(b) lifts the droplet toward the nodal plane and qualitatively transforms the streaming flow into a principally dipolar motif. This transition from quadrupolar to dipolar flow has been with increasing trap stiffness has been predicted analytically and is reported in Fig. 7 of Ref. [14]. Further increasing the trap stiffness in Fig. 5(c) lifts the particle still closer to the nodal plane and induces second transition back to quadrupolar streaming that appears not to have been reported previously.

2. Deformable Droplets

Both dynamical transitions reported in Fig. 5 occur for droplets that are stiff enough to remain substantially spherical while trapped. This is consistent with the assumption of sphericity that underlies the analysis in Ref.¹⁴. Figure 6 reveals yet another dynamical transition that occurs when a strongly-trapped droplet is soft enough to deform, a scenario that has not been considered in previous studies. The droplet in Fig. 6(a) is comparable to the droplet in Fig. 5(c), except that its surface tension is smaller by a factor of two. The droplet consequently deforms into an ellipsoid under the uniaxial stress of the acoustic levitator and settles at a slightly different height relative to the nodal plane. The induced streaming flow nevertheless retains its quadrupolar nature.

Reducing the surface tension, in Fig. 6(b), increases the distortion and moves both the interior and exterior circulation closer to the droplet surface. Reducing the surface tension still further, in Fig. 6(c), suppresses the vortex structure entirely.

The streaming flow around the ellipsoid droplet is primarily dipolar. This deformation-induced dynamical transition also appears not to have been observed in prior studies. These observations illustrate the value of the hybrid IBM for probing the dynamical properties of insonated droplets.

V. DISCUSSION

We have introduced a hybrid immersed boundary method that efficiently models the stresses on acoustically levitated droplets and the surrounding fluid. We have validated our method by simulating a single droplet in a plane standing wave, and comparing the results with the best available analytical and numerical solutions. Even in this minimal system, the hybrid IBM reveals transitions between dipolar and quadrupolar streaming under strong-driving conditions that have not been reported in previous studies. These observations offer new insights into the response of deformable droplets to the forces and torques created by acoustic landscapes.

Compared to traditional compressible flow simulations, our hybrid method cuts computational cost by utilizing semi-analytic techniques to accommodate acoustic scattering in hydrodynamic simulations. The benefits are greatest when stress-induced deformations are small enough that analytic scattering calculations can be carried out rapidly. When the droplet shape is highly irregular and unpredictable, most known semi-analytic techniques converge slowly and may be prohibitively expensive. However, for droplets with small to moderate deformations, the hybrid IBM may be up to three orders of magnitude faster than compressible flow simulations. For the implementation presented here, the hybrid method efficiently and effectively models complex shape deformations and streaming profiles around a single droplet, and can easily be scaled up to study acoustohydrodynamic interactions among multiple particles.

The framework presented here is, by design, extremely flexible. If necessary, the accuracy of the hybrid IBM can be improved by introducing more advanced scattering solutions for Eq. (18), implementing viscous waves from Eq. (13b), or even adding additional pairwise acoustic forces, like the Bjerknes force⁵. Or, as in this work, inexpensive approximations can be used throughout to efficiently model qualitative behaviors.

ACKNOWLEDGMENTS

This work was supported by the National Science Foundation under Award Number DMR-2104837.

We are grateful to professor Charles Peskin for extensive discussions on the formulation of the Immersed Boundary Method.

DATA AVAILABILITY

The data that support the findings of this study are available from the corresponding author upon reasonable request.

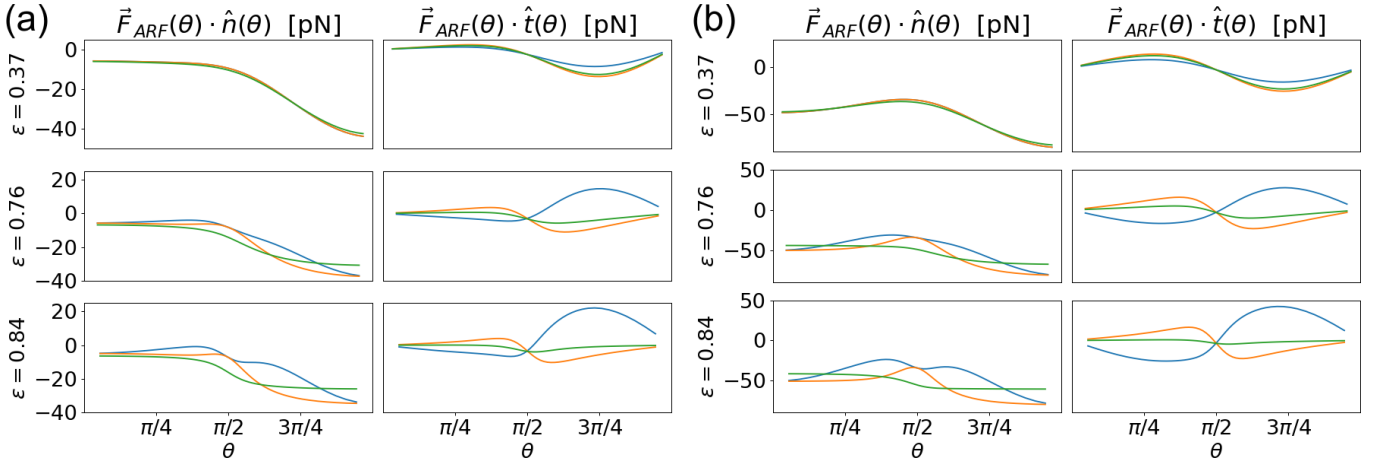


FIG. 8. Normal and tangential components of the acoustic radiation force as a function of position, θ , on the droplet surface for ellipsoids of various eccentricities. (a) moderate displacement: $z_0 = -3.5 \mu\text{m}$. (b) larger displacement: $z_0 = -10.6 \mu\text{m}$. The ARF at the surface is calculated using the spherical fields from Eq. (21) (blue), the projection correction described in Eq. (26) (orange), and the exact analytic solution in spheroidal coordinates (green).

Appendix A: Flows around a sedimenting spherical droplet

Analytic solutions are available for the viscous flow fields inside and around a spherical fluid droplet as it moves with velocity $\mathbf{v} = v\hat{z}$ through an immiscible fluid²⁶. Assuming that the two fluids have the same viscosity, the stream functions inside and outside the droplet are

$$\psi^{(i)}(\mathbf{r}) = \frac{1}{8}vr^2 \left(\frac{r^2}{a_p^2} - 1 \right) \sin^2 \theta, \quad \text{and} \quad (\text{A1})$$

$$\psi^{(o)}(\mathbf{r}) = \frac{1}{8}v \frac{a_p^3}{r} \left(1 - 5 \frac{r^2}{a_p^2} \right) \sin^2 \theta, \quad (\text{A2})$$

respectively. The associated flow field is

$$\mathbf{u}(\mathbf{r}) = \nabla \times (\psi \hat{z}). \quad (\text{A3})$$

Appendix B: Applicability of the Scattering Approximation from Sec. III C

The approximation in Sec. III C is derived by assuming that the acoustic fields at the droplet surface, $r = S(\theta)$, are similar to that at a minimally enclosing sphere, $r = R \equiv \max[S(\theta)]$. The interior potential from Eq. (18a) can be rewritten by Taylor expanding the radial function to 1st order in $S - R$,

$$j_\ell(kS) = j_\ell(k_1R) + (S - R)k j'_\ell(k_1R) + \mathcal{O}\{(S - R)^2\}$$

In the long-wavelength limit, $kR \ll 1$, we can use the small-argument asymptotic form $j_\ell(z) \propto z^\ell$, and so we have

$$j_\ell(kS) = \left[1 + \ell \left(\frac{S}{R} - 1 \right) \right] j_\ell(k_1R) + \mathcal{O}\{(S - R)^2\}$$

so that $\phi_I(R) \approx \phi_I(S)$ as long as

$$\left(\frac{S}{R} - 1 \right) \ll \frac{1}{\ell}$$

for all non-negligible modes. Likewise, repeating this procedure for the scattered field reveals that $\phi_s(R) \approx \phi_s(S)$ when $\left(\frac{S}{R} - 1 \right) \ll 1/(\ell + 1)$.

Because the error in the radial function is also proportional to ℓ , higher modes are approximated more accurately than lower modes. Consequently, the applicability of this method also depends on the local structure of the acoustic field. In this work, we have shown in Fig. 4 that our approximation performs well even at moderately large deformations, when the droplet is close to the node. However, as illustrated by Fig. 8, the range of validity is restricted to smaller deformations when the droplet is farther away from the node.

¹S. Santesson and S. Nilsson, “Airborne chemistry: acoustic levitation in chemical analysis,” *Anal. Bioanal. Chem.* **378**, 1704–1709 (2004).

²M. A. Andrade, N. Pérez, and J. C. Adamowski, “Review of progress in acoustic levitation,” *Braz. J. Phys.* **48**, 190–213 (2018).

³C. Mu, J. Wang, K. M. Barraza, X. Zhang, and J. L. Beauchamp, “Mass spectrometric study of acoustically levitated droplets illuminates molecular-level mechanism of photodynamic therapy for cancer involving lipid oxidation,” *Angew. Chem., Int. Ed. Engl.* **58**, 8082–8086 (2019).

⁴A. Marzo and B. W. Drinkwater, “Holographic acoustic tweezers,” *PNAS* **116**, 84–89 (2019).

⁵M. A. Abdelaziz, J.-L. Aider, D. J. Pine, D. G. Grier, M. Hoyos, *et al.*, “Ultrasonic chaining of emulsion droplets,” *Phys. Rev. Res.* **3**, 043157 (2021).

⁶G. T. Silva and B. W. Drinkwater, “Acoustic radiation force exerted on a small spheroidal rigid particle by a beam of arbitrary wavefront: Examples of traveling and standing plane waves,” *J. Acoust. Soc. Am.* **144**, EL453–EL459 (2018).

⁷J. T. Karlsen and H. Bruus, “Forces acting on a small particle in an acoustic field in a thermoviscous fluid,” *Phys. Rev. E* **92**, 043010 (2015).

⁸L. Wang, F.-B. Tian, and J. C. Lai, “An immersed boundary method for fluid–structure–acoustics interactions involving large deformations and complex geometries,” *J. Fluids Struct.* **95**, 102993 (2020).

⁹H. Bruus, “Acoustofluidics 7: The acoustic radiation force on small particles,” *Lab Chip* **12**, 1014–1021 (2012).

¹⁰W. L. Nyborg, “Acoustic streaming near a boundary,” *J. Acoust. Soc. Am.* **30**, 329–339 (1958).

¹¹Q. Qi, “The effect of compressibility on acoustic streaming near a rigid boundary for a plane traveling wave,” *J. Acoust. Soc. Am.* **94**, 1090–1098 (1993).

- ¹²C. P. Lee and T. G. Wang, "Outer acoustic streaming," *J. Acoust. Soc. Am.* **88**, 2367–2375 (1990).
- ¹³P. J. Westervelt, "The theory of steady rotational flow generated by a sound field," *J. Acoust. Soc. Am.* **25**, 60–67 (1953).
- ¹⁴T. Baasch, A. A. Doinikov, and J. Dual, "Acoustic streaming outside and inside a fluid particle undergoing monopole and dipole oscillations," *Phys. Rev. E* **101**, 013108 (2020).
- ¹⁵P. L. Marston, "Shape oscillation and static deformation of drops and bubbles driven by modulated radiation stresses—theory," *J. Acoust. Soc. Am.* **67**, 15–26 (1980).
- ¹⁶H. Bruus, "Acoustofluidics 2: Perturbation theory and ultrasound resonance modes," *Lab Chip* **12**, 20–28 (2012).
- ¹⁷F. Mitri, "Axial acoustic radiation force on rigid oblate and prolate spheroids in bessel vortex beams of progressive, standing and quasi-standing waves," *Ultrasonics* **74**, 62–71 (2017).
- ¹⁸P. Waterman, "T-matrix methods in acoustic scattering," *J. Acoust. Soc. Am.* **125**, 42–51 (2009).
- ¹⁹C. S. Peskin, "Flow patterns around heart valves: a numerical method," *J. Comput. Phys.* **10**, 252–271 (1972).
- ²⁰C. S. Peskin, "The immersed boundary method," *Acta numerica* **11**, 479–517 (2002).
- ²¹S. Maramizonouz, M. Rahmati, A. Link, T. Franke, and Y. Fu, "Numerical and experimental studies of acoustic streaming effects on microparticles/droplets in microchannel flow," *Int. J. Eng. Sci.* **169**, 103563 (2021).
- ²²Y. Kim and C. S. Peskin, "Penalty immersed boundary method for an elastic boundary with mass," *Phys. Fluids* **19**, 053103 (2007).
- ²³Y. Kim and C. S. Peskin, "A penalty immersed boundary method for a rigid body in fluid," *Phys. Fluids* **28**, 033603 (2016).
- ²⁴T. G. Fai, B. E. Griffith, Y. Mori, and C. S. Peskin, "Immersed boundary method for variable viscosity and variable density problems using fast constant-coefficient linear solvers i: Numerical method and results," *SIAM J. Sci. Comput.* **35**, B1132–B1161 (2013).
- ²⁵Y. Kim and C. S. Peskin, "Numerical study of incompressible fluid dynamics with nonuniform density by the immersed boundary method," *Phys. Fluids* **20** (2008).
- ²⁶J. Happel and H. Brenner, *Low Reynolds Number Hydrodynamics: with Special Applications to Particulate Media*, Vol. 1 (Springer Science & Business Media, 1983).
- ²⁷M. Settles and H. Bruus, "Forces acting on a small particle in an acoustical field in a viscous fluid," *Physical Review E* **85**, 016327 (2012).
- ²⁸S. Danilov and M. Mironov, "Mean force on a small sphere in a sound field in a viscous fluid," *J. Acoust. Soc. Am.* **107**, 143–153 (2000).
- ²⁹P. J. Westervelt, "Acoustic radiation pressure," *J. Acoust. Soc. Am.* **29**, 26–29 (1957).
- ³⁰G. T. Silva, "An expression for the radiation force exerted by an acoustic beam with arbitrary wavefront (I)," *J. Acoust. Soc. Am.* **130**, 3541–3544 (2011).
- ³¹W. L. M. Nyborg, "Acoustic streaming," in *Physical acoustics*, Vol. 2 (Elsevier, 1965) pp. 265–331.
- ³²M. A. Yurkin and A. G. Hoekstra, "The discrete dipole approximation: an overview and recent developments," *J. Quant. Spectrosc. Radiat. Transf.* **106**, 558–589 (2007).
- ³³F. G. Mitri, "Axisymmetric scattering of an acoustical bessel beam by a rigid fixed spheroid," *IEEE Trans. Ultrason. Ferroelectr. Freq. Control* **62**, 1809–1818 (2015).
- ³⁴L. Wang and F.-B. Tian, "Numerical study of sound generation by three-dimensional flexible flapping wings during hovering flight," *J. Fluids Struct.* **99**, 103165 (2020).
- ³⁵J. H. Seo and R. Mittal, "A high-order immersed boundary method for acoustic wave scattering and low-mach number flow-induced sound in complex geometries," *J. Comput. Phys.* **230**, 1000–1019 (2011).
- ³⁶E. H. Trinh and C.-J. Hsu, "Equilibrium shapes of acoustically levitated drops," *J. Acoust. Soc. Am.* **79**, 1335–1338 (1986).
- ³⁷H. Jackson, M. Barmatz, and C. Shipley, "Equilibrium shape and location of a liquid drop acoustically positioned in a resonant rectangular chamber," *J. Acoust. Soc. Am.* **84**, 1845–1862 (1988).
- ³⁸P. L. Marston, S. E. LoPorto-Arione, and G. L. Pullen, "Quadrupole projection of the radiation pressure on a compressible sphere," *J. Acoust. Soc. Am.* **69**, 1499–1501 (1981).